Interactions between nanoscale zerovalent iron (NZVI) and silver nanoparticles alter the NZVI reactivity in aqueous environments

J. Deng, S. Yoon, M. Pasturel, S. Bae, Khalil Hanna

Interactions between nanoscale zerovalent iron (NZVI) and silver nanoparticles alter the NZVI reactivity in aqueous environments

Junmin Deng[1], Sunho Yoon[2], Mathieu Pasturel[3], Sungjun Bae[2*], Khalil Hanna[1*]

[1] *Univ. Rennes, Ecole Nationale Supérieure de Chimie de Rennes, CNRS, ISCR-UMR 6226, F-35000 Rennes, France*

[2] *Department of Civil and Environmental Engineering, Konkuk University, 120 Neungdong-ro, Gwangjin-gu, Seoul 05029, Republic of Korea*

[3] *Univ. Rennes, CNRS, ISCR – UMR 6226, F-35000 Rennes, France*

*Co-corresponding authors: khalil.hanna@ensc-rennes.fr and bsj1003@konkuk.ac.kr

ABSTRACT

The increasing production and broad application of engineered nanoparticles (ENPs) have led to a substantial release of ENPs into natural systems. Despite their different utilization prospects, ENPs such as nanoscale zero-valent iron (NZVI) and silver nanoparticles (AgNPs) have been co-found in aquatic environments. This study comprehensively examined the effect of AgNPs on the reductive ability of NZVI, which was probed through the conversion of *p*-nitrophenol (*p*-NP) to *p*-aminophenol (*p*-AP). Electron microscopic and spectroscopic investigations and Derjaguin–Landau–Verwey–Overbeek (DLVO) calculations showed that the aggregation of NZVI with a low dose of AgNPs dramatically decreased the NZVI reactivity. In contrast, enhanced NZVI reactivity was observed when a high dose of AgNPs was used. The collision between self-assembled aggregates of AgNPs and NZVI can lead to the exposure of inner Fe(0), thereby improving the reductive ability of NZVI. The same behavior was observed for other nanosized (e.g., TiO_2) and microsized (e.g., quartz sand) particles, which suggests the predominance of physical processes in NZVI peeling. Further investigations showed that the presence of sulfate and humic acid enhanced the *p*-NP removal in the NZVI-AgNP suspension, in contrast to other groundwater constituents. Our findings provide a better understanding of potential ENP interactions, particularly in the context of groundwater remediation.

Keywords: nanoscale zerovalent iron; silver nanoparticles; *p*-nitrophenol; aggregation.

Graphical Abstract

Interactions between nanoscale zero-valent iron (NZVI) and silver nanoparticles (AgNPs) significantly alter the reductive ability of NZVI

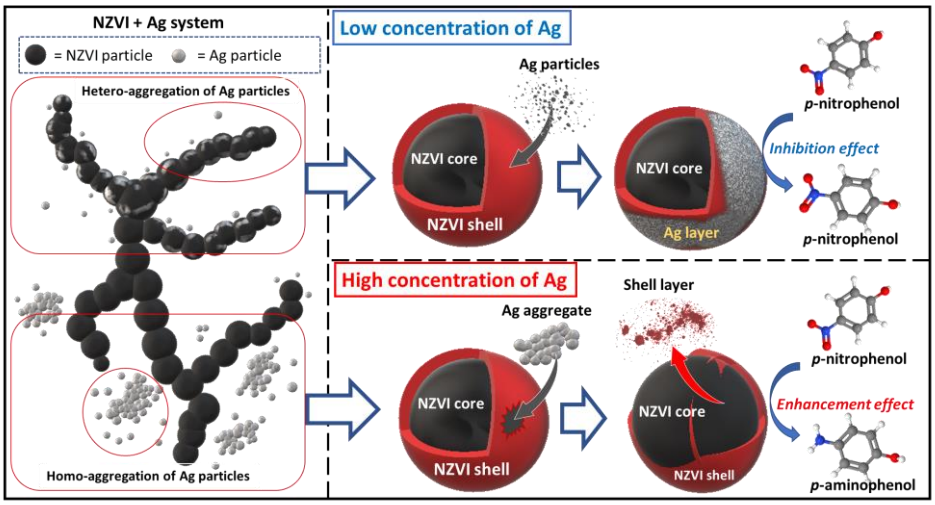

1. Introduction

Over the past decades, due to increasing production and broad applications of engineered nanoparticles (ENPs), such as textile (Lorenz et al., 2012), electronics (Poudel and Kim, 2022; Poudel et al., 2021), pharmaceuticals (Sridhar et al., 2015), environmental remediation (Poudel et al. 2022) and cosmetics (Auffan et al., 2010), a significant amount of ENPs are ended up into natural systems (Abbas et al., 2020; Danail and Ineke, 2009). In particular, silver nanoparticles (AgNPs) are one of the most commonly used ENPs. Their catalytic ability, high surface area to volume ratio and antibacterial activity provide them with excellent potential for various industrial (Poudel et al., 2020; Shen et al., 2014), food (Echegoyen and Nerín, 2013) and medical applications (Deng et al., 2016). However, their release and accumulation in the environment (water and soil) (McGillicuddy et al., 2018; Mahdi et al., 2017) is of concern owing to their potential adverse effects on human health and aquatic life (Asghari et al., 2012; Xu et al., 2013). In the meanwhile, nanoscale zero-valent iron (NZVI), as one of the most extensively used ENPs, has been widely applied for groundwater remediation and wastewater treatment because of its high reactivity, cost-effectiveness, and environmental friendliness (Li et al., 2017; Phenrat et al., 2016; Wei et al., 2010; Xia et al., 2017). NZVI can be used to treat various contaminants such as persistent organic pollutants (Joo et al., 2004), toxic inorganic contaminants (Ryu et al., 2011) and even radioactive nuclides (Tsarev et al., 2017).

When AgNPs are discharged into terrestrial or aquatic environments, their

66 interaction with other co-existing ENPs could influence their environmental behavior,
67 fate, and likely their ecotoxicity. In addition, AgNPs can potentially alter the reactivity
68 of other ENPs used for decontamination, such as NZVI. The injection of NZVI slurry
69 is a common method for the *in situ* remediations of aquifer and groundwater
70 contamination by organic or inorganic compounds (Su et al., 2013; Mueller et al., 2012).
71 Despite the possible co-occurrence of both ENPs in aquatic environments (Stefaniuk et
72 al., 2016; Syafiuddin et al., 2018), there is a lack of knowledge on their potential
73 interactions. Therefore, a comprehensive study on the interactions between NZVI and
74 AgNPs is needed considering the contaminant removal methods used in remediation
75 processes.

76 Herein, we selected *p*-nitrophenol (*p*-NP), as a probe compound because the
77 reductive conversion of *p*-NP to *p*-aminophenol (*p*-AP) is well documented, and the
78 corresponding mass balance is easy to establish owing to the low adsorption of
79 nitrophenol and aminophenol by metal oxides (Bae et al., 2016; Lai et al., 2014; Vilardi
80 2020). In order to investigate the interactions between NZVI and AgNPs and clearly
81 highlight specific effects of AgNPs on the NZVI reductive ability, we applied a wide
82 concentration range and high-enough dosage of AgNPs (0.5 − 100 mg/L) in NZVI
83 suspension. Two concentrations of NZVI (25 and 50 mg/L) within the concentration
84 range typically used in lab-experiments were investigated. The phase transformation
85 and morphological change of NZVI and AgNPs were monitored by X-ray diffraction
86 (XRD), X-ray photoelectron spectroscopy (XPS), and transmission electron

microscopy (TEM) with energy-dispersive X-ray spectroscopy (EDS). In addition, a theoretical investigation based on Derjaguin–Landau–Verwey–Overbeek (DLVO) calculations were conducted for the low and high doses of AgNPs. Moreover, to get more insight into the relationship between effects of ENPs and their nature, interactions of NZVI with other widely used ENPs (e.g. nanosized TiO_2 particles) and inert mineral surface (e.g. quartz sand) were also investigated. Finally, the NZVI-AgNP interactions were evaluated in the presence of naturally occurring anions and cations and natural organic matter, at levels similar to those encountered in real groundwater.

2. Materials and methods

2.1 Chemicals and materials

Sodium borohydride ($NaBH_4$, ≥99.0%), *p*-NP (≥99%), *p*-AP (≥98%), ferric chloride hexahydrate ($FeCl_3 \cdot 6H_2O$, ≥99.0%), hydrochloric acid (HCl, 37%), sodium hydroxide (NaOH, ≥99.0%), sodium chloride (NaCl, ≥99.5%), sodium sulfate (Na_2SO_4, ≥99.0%), calcium chloride ($CaCl_2$, ≥99.9%), magnesium chloride ($MgCl_2$, ≥98.0%) and sodium metasilicate nonahydrate ($Na_2SiO_3 \cdot 9H_2O$, ≥98.0%) were purchased from Sigma-Aldrich, France. Acetonitrile (99.99%, Sigma) and acetic acid (99.7%, ACROS) were used as the mobile phase for the high-performance liquid chromatography (HPLC) analysis. Leonardite humic acid (LHA) standard was purchased from the International Humic Substances Society (IHSS). Silver nano-powder (containing polyvinylpyrrolidone (PVP) as a dispersant, 99.5%, <100 nm, and PZC ~3.3) and TiO_2

nano-powder (rutile, 99.5%, 50 m^2/g, <100 nm, and PZC ~5.9) were purchased from Sigma-Aldrich. Fontainebleau quartz sand (FB sand, 0.06 m^2/g, 150–300 μm, PZC ~2.7) was obtained from VWR International. Based on a previously published method (Deng et al., 2020), NZVI was synthesized by reducing 0.11 M $FeCl_3 \cdot 6H_2O$ with 0.9 M $NaBH_4$ in an anaerobic chamber.

The glassware was soaked in 5% (v:v) HCl for at least 48 h and rinsed before use. Unless specifically stated, all solutions were prepared with deoxygenated deionized water (DDIW, 18.2 MΩ·cm), purged with nitrogen (N_2, 99.99%) for 4 h, and stored in an anaerobic chamber (JACOMEX).

2.2. Experimental and analytical methods

Batch experiments were conducted in 500 mL flask in an anaerobic chamber under dark conditions. An exact amount of NZVI (0.0125 and 0.025 g) was transferred to the flask containing 500 mL of DDIW, and the mixture was stirred at 500 rpm to prepare the samples with initial NZVI concentrations of 25 and 50 mg/L. To monitor the variations in pH and oxidation-reduction potential (ORP) throughout the experiment, we used a portable pH–ORP meter (HI991003, Hanna). After 1 h, AgNPs were introduced into the suspensions to form a mixture of NZVI and AgNPs at different Ag concentrations (0.5, 2, 10, 25, 50, and 100 mg/L). An equilibration time of 1 hour was chosen because pH and ORP values have reached constant values after 1 h of reaction time. Although this time is sufficient to obtain an equilibrated NZVI suspension under our

129 experimental conditions, it may not be applicable at the field-scale.

130 After 15 h, pH and ORP reached an equilibrium, and 2 mL of *p*-NP stock solution
131 (25 mM) was added to the suspension to initiate the reaction with *p*-NP (0.1 mM).
132 Subsequently, 1 mL samples were withdrawn from the suspension and then filtered
133 through a 0.2 μm filter (Whatman) for HPLC analysis. The aqueous concentrations of
134 *p*-NP and *p*-AP were determined using HPLC (Waters 600 controller) with a photodiode
135 array detector (Waters 996) and a reversed-phase C18 column (250 mm × 4.6 mm i.d.,
136 5 μm). A mobile phase (acetonitrile: water at 50:50 (v:v)) containing 0.1% formic acid
137 was prepared and used at a flow rate of 1 mL/min in isocratic mode. In addition, mass
138 balance of *p*-NP and *p*-AP after reaction was checked and presented in Table S1.

139 The same procedure was used to investigate the effects of TiO_2 nanoparticles, FB
140 sand, and groundwater solutes on the reactivity of NZVI and NZVI/AgNPs. The AgNP
141 dissolution experiments were conducted at pH 9 in absence of NZVI, which is similar
142 to the working pH in presence of NZVI, at AgNP dosage of 0.5, 2, 10, 25, 50, and 100
143 mg/L. Although the dosage of AgNPs seems to be higher than the frequently detected
144 concentration in natural systems, we have assessed the interactions of NZVI with
145 AgNPs over a wide range of Fe/Ag ratios (0.5 - 50) to cover some environmentally-
146 relevant scenarios.

147 After 3 d, the samples were filtered through a 0.2 μm filter to measure the amount
148 of Ag^+ ions by inductively coupled plasma mass spectrometry (ICP-MS, Agilent 7700x).
149 All experiments were performed in triplicates. The data reported here are the average

of three replicated experiments, and the error bars represent the relative standard deviation.

2.3. Characterization

XRD (D8, BRUKER) was used to identify the resulting products of NZVI after reaction with *p*-NP. The resulting suspensions were first collected and washed with DDIW three times, and dried in a vacuum freeze drier (−52 °C, 24 h). The dried samples were then transferred to sample holders and treated with 1:1 (v:v) glycerol solution to avoid surface oxidation during the XRD analysis (Bae and Lee, 2014). XPS (Sigma Probe system, Thermo) analysis was performed for NZVI, AgNPs, and NZVI-AgNP samples. The power source (Al Kα X-ray, 1486.7 eV) was 75 W, and the C 1s peak at 285 eV was used as a reference for the correction of surface charging effects. The morphological characterization of the NZVI and NZVI-AgNP mixtures was performed by TEM–EDS, (JEM-2100, JEOL). The average particle size of the NZVI-AgNP suspension with groundwater solutes and the zeta potential of induvial particles (i.e., NZVI and AgNPs) were measured using a Zetasizer (Matec Applied Sciences). The average hydrodynamic diameter of AgNPs and NZVI were determined using time-resolved dynamic light scattering (DLS, ALV-5000, Langen).

3. Results and discussion

3.1 Effect of AgNPs on the NZVI reactivity

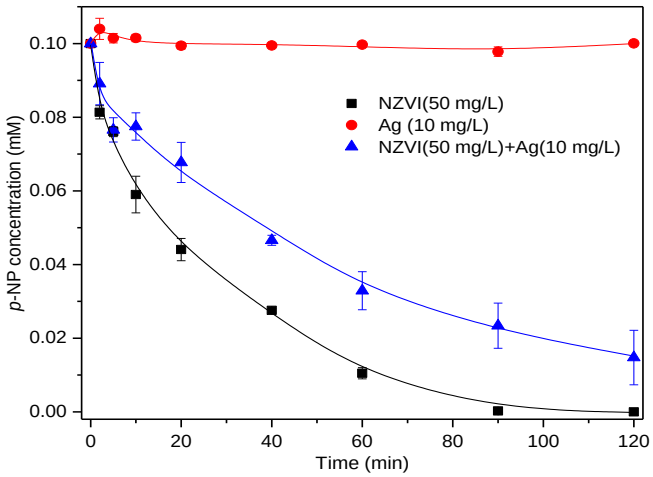

171

172 Figure 1. Concentrations of *p*-NP during the removal of *p*-NP by different nanoparticles.
173 Experimental conditions: $[p\text{-NP}]_{initial}$ = 0.1 mM; [NZVI] = 50 mg/L; [AgNPs] = 10
174 mg/L; pH = 9.0±0.2.

175

176 The interactions between AgNPs and NZVI were investigated under anoxic
177 conditions by monitoring the variations in pH and ORP throughout the experiment,
178 including at i) the addition of NZVI to the reactor, ii) addition of AgNPs, and iii)
179 removal of *p*-NP (see Supporting Information (SI), Fig. S1). When NZVI was added to
180 water at 50 mg/L (i.e., first 1 h), there was a clear increase in pH from 6.78 to 9.38 and
181 a decrease in ORP from −54 to −843 mV, which were attributed to the reaction between
182 NZVI and water (Bae and Hanna, 2015). After the addition of AgNPs at 10 mg/L to the
183 NZVI suspension, the pH and ORP values remained constant, and only slight changes
184 were observed in the pH and ORP after 15 h of reaction. The slight decreasing in pH
185 and increasing in ORP value may be attributed to the consumption of Fe^{2+} and OH^- by

186 the hydrolysis of ferrous under alkaline conditions (Deng et al., 2020). Afterward, little
187 variations in pH or ORP were observed during the *p*-NP removal. Only a slight decrease
188 in pH and increase in ORP was observed upon the addition of the *p*-NP solution.
189 The removal of *p*-NP by various materials, including NZVI alone, AgNPs alone,
190 and NZVI/AgNPs mixture, was also evaluated (Fig. 1). Since the standard potential of
191 Ag^0/Ag^+ and p-NP/p-AP is 0.79 V and 0.76 V respectively, the conversion of *p*-NP to
192 *p*-AP by AgNPs is not likely to take place spontaneously (Hernández-Gordillo et al.
193 2014). Indeed, no *p*-NP removal was observed in the AgNP suspension, which indicated
194 negligible adsorption and/or reduction of *p*-NP by AgNPs. In contrast, the complete
195 removal of *p*-NP was observed after 90 min of reaction with NZVI, whereas 85% of *p*-
196 NP was removed by the NZVI-AgNP suspension over 120 min. The mass balance was
197 evaluated, which confirmed the reductive conversion of *p*-NP to *p*-AP (not shown) and
198 the negligible adsorption of *p*-NP and *p*-AP on the NZVI surface. It is reported that the
199 hydrogen production caused by anaerobic corrosion of NZVI could potentially affect
200 the reduction of target contaminants (Liu and Lowry, 2006). However, the working pH
201 was 9 in our experiments, which significantly decrease the generation of hydrogen gas
202 (Liu and Lowry 2006). In addition, it has been generally accepted that the active H atom
203 seems to be readily captured by reactive catalysts (e.g., Ni) rather than Fe phase, and
204 reduction of *p*-NP could not be occurred by dissolved hydrogen alone (Du et al. 2004).
205 Therefore, hydrogen contribution should be of minor importance in our reaction
206 systems.

The effect of varying AgNP concentrations (0.5−100 mg/L) on the *p*-NP removal by NZVI (25 and 50 mg/L) was then investigated (Fig. S2). Nearly 72% of *p*-NP was removed by 25 mg/L of NZVI after 8 h, whereas the addition of 0.5 mg/L of AgNPs to the NZVI suspension decreased the removal to 62%. An increase in the AgNP concentration resulted in a gradual increase in the conversion of *p*-NP to *p*-AP (i.e., 64% at 2 mg/L, 84% at 10 mg/L, 89% at 25 mg/L, and 93% at 50 mg/L) (Fig. S2(a)). Similarly, the removal efficiency of *p*-NP after 2 h of reaction significantly decreased when 0.5 mg/L of AgNPs was added to a 50 mg/L NZVI suspension, and it continuously increased as the AgNP content increased (Fig. S2(b)).

To further demonstrate the variations in removal rate, we plotted the removal kinetics fitted using the pseudo-first-order equation over the early reaction stage (60 min) and the removal rate constants (k_{obs}) against AgNP dose (Fig. 2 and Fig. S2(c) and (d)). Compared to NZVI alone (0.0085 min^{-1} at 25 mg/L, and 0.037 min^{-1} at 50 mg/L), the obtained rate constant was nearly 1.5 and 5.8 times lower after the addition of 0.5 mg/L AgNPs. However, the k_{obs} values gradually increased to 0.0131 and 0.042 min^{-1} as the AgNP dose increased, at 25 and 50 mg/L NZVI, respectively. Therefore, the results showed that the presence of AgNPs at a low dose significantly inhibited the NZVI reactivity, but this inhibitive effect gradually disappeared as the AgNP concentration increased.

To verify whether this two-step phenomenon was specific to AgNPs, additional investigations were conducted with nanosized TiO_2 particles (used as active

228 nanoparticles) and microsized quartz sand particles (used as an inert surface) under dark
229 conditions. For TiO_2, the inhibition of *p*-NP removal was observed at a low dosage (5
230 mg/L), whereas an increase in TiO_2 dose enhanced the *p*-NP reduction (Fig. S3). It is
231 worth noting that TiO_2 alone showed negligible removal of *p*-NP at pH 9 (See Fig. S4),
232 suggesting that possible adsorption of *p*-NP on TiO_2 can be excluded under our
233 experimental conditions. However, the addition of quartz sand showed a one-step
234 behavior, that is, the removal rate constant continuously increased with increasing sand
235 dose (Fig. S5). Collectively, these results suggest that the increase or decrease in *p*-NP
236 removal rate was not limited to the effect of AgNPs, and it likely resulted from a
237 combination of physical and chemical processes.

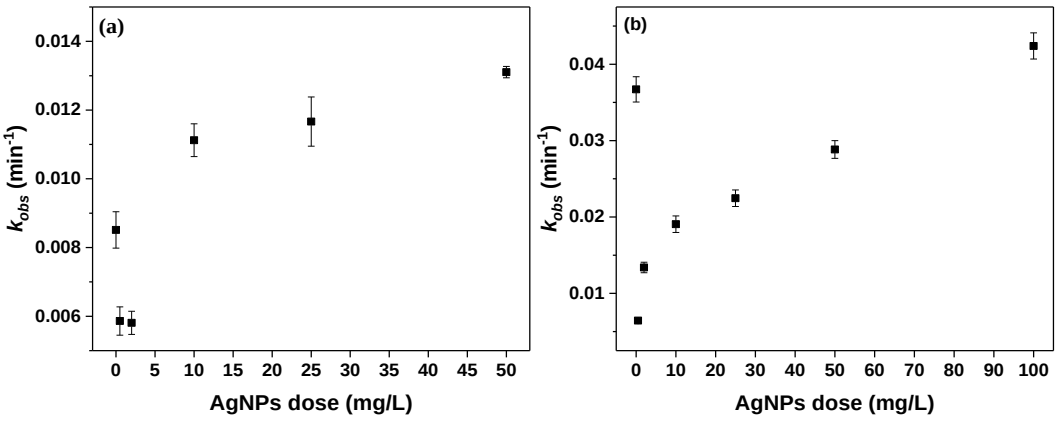

238

239 Figure 2. Variation in pseudo-first-order kinetic rate constants (k_{obs}, min^{-1}) of the
240 removal of *p*-NP by NZVI with respect to AgNP dosage at (a) 25 mg/L NZVI and (b)
241 50 mg/L NZVI. Experimental conditions: $[p\text{-NP}]_{initial}$ = 0.1 mM; pH = 9.0±0.2.

242

243 *3.2 Heteroaggregation and homoaggregation of AgNPs*

244 The kinetic experiments suggested that the NZVI reactivity can be altered by the
245 interactions between AgNPs and NZVI, which might be caused by potential
246 aggregation and/or redox reactions between the two particles. As previously observed
247 for goethite and hematite (Wang et al., 2019), AgNPs might bind to the surface of the
248 oxides layer in the core-shell structure of NZVI. Accordingly, the electrostatic attraction
249 between negatively charged AgNPs (PZC ~3.3) and iron oxides has been used to
250 explain the heteroaggregation process and inhibition of AgNP dissolution (Wang et al.,
251 2019). However, these interactions have been investigated at circumneutral pH values
252 (5.5 and 7.5), at which the surface charge of goethite (PZC ~ 9) and hematite (PZC ~ 8)
253 are predominately positive. This emphasizes the role of electrostatic attraction for the
254 adsorption of negatively charged AgNPs onto iron oxides. The zeta potential of NZVI
255 and AgNPs at different pHs were measured to gain more insight into electrostatic
256 interactions between the two types of particle (Fig. S6). However, the working pH of
257 the NZVI suspension lay at 9, at which the surface charge of both NPs are negative.
258 Indeed, at pH above the PZC of minerals, dissociation of surface functional groups in
259 water will give a negatively charged surface (Lützenkirchen et al. 2008).
260 To investigate the interparticle interactions in NZVI-AgNP suspensions under the
261 experimental conditions of the present work, TEM–EDS analyses were conducted. The
262 silver nanoparticles sample used in this study is mostly round shape with particle size
263 in water lower than 100 nm. The NZVI showed chain-like aggregates consisting of
264 spherical particles (60–100 nm) (Fig. 3(a)), which are generally attributed to the high

surface energy and intrinsic magnetic interaction among NZVI particles (Sohn et al., 2006). Significantly smaller particles were attached to larger particles (80–100 nm) when 10 mg/L of AgNPs was added (Fig. 3(b)). However, the attachment of small particles was not observed at a high AgNP dose (100 mg/L) (Fig. 3(c)). Instead, we observed the co-existence of chain-like aggregates and nanoparticle assemblages. The EDS mapping of NZVI-AgNP mixtures showed distinct Fe and Ag nanoparticles highlighted in red and green, respectively, in Figs. 3(d) and (e). As illustrated in Fig. 3(d), the Ag-phase was enriched near the surface of Fe aggregates at low AgNP concentrations, which suggests the heteroaggregation of NZVI and AgNPs. The spatial correlation of Ag and Fe was not observed at high AgNP concentrations (Fig. 3(e)), but these two elements existed in different locations because AgNPs tended to homoaggregate rather than interact with NZVI at higher AgNP doses. It was previously reported that aggregation behavior of NPs would change along with their oxidation (Vilardi 2019, Vilardi et al. 2019). However, similar TEM images of AgNPs and NZVI were observed after the reaction with *p*-NP (Fig. S7), suggesting no significant modification of the interactions between NZVI and AgNPs.

The enlarged TEM images with EDS mapping revealed a clear difference for different AgNP dosages (Fig. S8). In the absence of AgNPs (Fig. S8(a)), the TEM images of NZVI showed a typical shape of NZVI particles covered by a thin Fe oxide shell. The corresponding elemental mapping (Fe and O) further displayed the core-shell structure of NZVI, showing a strong signal intensity of Fe in the core, whereas O was

mostly present in the shell layer (2.5−3.5 nm). However, the thickness of the NZVI oxide shell seems to decrease significantly after the addition of 100 mg/L AgNPs, whereas almost no change was observed with the addition of 10 mg/L AgNPs. Based on the TEM–EDS results, we hypothesized that AgNPs at a low dose attach to the NZVI surfaces (i.e., iron oxides), and at a high dose, they tend to homoaggregate. We also hypothesized that introducing a high dosage of AgNP would lead to a decrease in the thickness of the NZVI oxide layer, which should be further investigated.

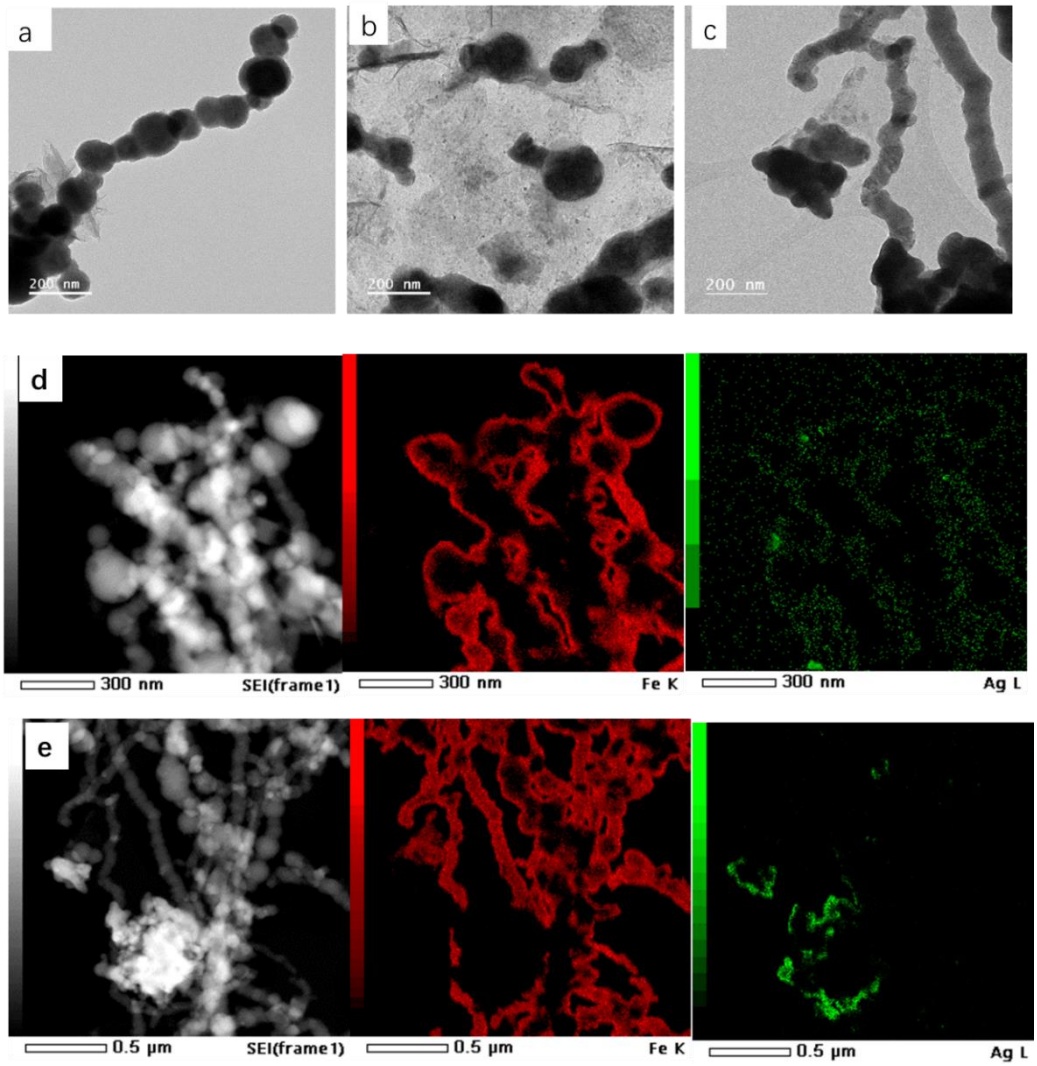

Figure 3. TEM images of (a) NZVI, (b) AgNP–NZVI at 10 mg/L AgNPs, and (c)

AgNP–NZVI at 100 mg/L AgNPs. Elemental mapping of AgNP–NZVI at AgNP doses of (d) 10 mg/L and (e) 100 mg/L. Conditions: [NZVI] = 50 mg/L.

We also analyzed the attraction and repulsion behaviors of AgNPs and NZVI according to the DLVO theory. This theory considers attractive van der Waals (vdW) and repulsive electrostatic double-layer (EDL) forces between the particles ($\Phi_{DLVO} = \Phi_{EDL} + \Phi_{vdW}$). The details of DLVO calculations are provided in the SI. In brief, at a low AgNP dose (10 mg/L), heteroaggregation (AgNP–NZVI) is likely to occur because of the lower repulsive energy barriers of AgNP–NZVI with respect to AgNP–AgNP. In addition, the AgNPs used in this study also contained stabilized PVP, so the surface coatings could serve as a bridge between coated AgNPs and uncoated NZVI to overcome the energy barrier (Lin et al., 2012). Therefore, it is likely that PVP-stabilized AgNPs formed heteroaggregates with NZVI. In contrast, a higher AgNP dose (100 mg/L) led to a significantly higher magnitude of calculated maximum repulsive interaction energies (Φ_{max}), which would not be sufficient to overcome non-DLVO energy. According to the calculations, neither heteroaggregation nor homoaggregation (AgNP–AgNP) would occur spontaneously. However, AgNP homoaggregation was still observed using TEM–EDS. This discrepancy between DLVO calculations and TEM images might be attributed to the potential chemical interactions between AgNPs and NZVI or oxide layer coating NZVI.

A recent study reported that AgNP morphology may change from a dispersed

316 spherical shape to larger aggregates owing to the release of Ag^+ possibly because of (i)
317 the nano bridges created by adsorption and/or redox conversion of Ag^+ into Ag^0 at the
318 particle surface to connect nearby particles, and (ii) the growth of reformed small
319 AgNPs around old AgNPs (Yu et al., 2014). Other reports showed that Ag^+ released
320 from AgNPs and possible electron transfer from Fe^0 to Ag^+ could form a galvanic
321 couple, which may accelerate NZVI-water corrosion (Zhuang et al., 2011; Zhu et al.,
322 2021). Therefore, interactions of Ag^+ ions (E_0 Ag/Ag^+ 0.799 V) with NZVI (E_0 Fe/Fe^{2+}
323 0.44 V) and AgNPs through adsorption and/or electron transfer processes may alter the
324 particle aggregation behavior and surface reactivity. In the present work, we have
325 measured Ag^+ ions in AgNP aqueous suspension but in the absence of NZVI, to avoid
326 sorption of released Ag+ ions on iron oxide layer of NZVI surface. As a result, these
327 dissolution tests were performed under oxic (open atmosphere) or mild reducing
328 conditions (anaerobic chamber), since the strong reducing conditions are ensured by
329 the presence of NZVI. Under such conditions, Ag^+ can be detected, and released
330 concentration was increased with increasing AgNP dose (See Fig. S10). However,
331 examination of the thermodynamic database by means of Eh-pH diagrams of Ag species
332 suggests that ions released through metal corrosion should be very limited, or even
333 excluded, under the experimental conditions of this study (pH 9, -800 mV) (Brookins,
334 1988). Indeed, no ions can be detected at alkaline pH values and strongly reducing
335 conditions, thereby ruling out galvanic effects between Ag^+ ions and inner Fe^0 within
336 iron oxide shell. In addition, the same two-step behavior in NP removal kinetics by

337 NZVI was observed when AgNP has been replaced by TiO_2 (Fig. S3), further
338 confirming the minor role of ions release and/or galvanic effect in the investigated
339 systems.

340 Collectively, these results suggest that heteroaggregation of NZVI-AgNPs which
341 is favorable at lower AgNP dose owing to the relatively lower energy barrier may alter
342 the NZVI reactivity. As the AgNP dose increased, AgNP homoaggregation can be
343 expected, thereby preventing potential alteration of the initial NZVI reactivity.

344

345 *3.3. Spectroscopic investigations*

346 To investigate the oxidation states of Ag and Fe in AgNP and NZVI suspensions,
347 the XPS spectra of the Ag(3d) and Fe(2p) bands of AgNP, NZVI, and NZVI-AgNP
348 suspensions were analyzed (Fig. 4). For AgNPs and NZVI-AgNPs, the $Ag(3d_{5/2})$ and
349 $Ag(3d_{3/2})$ peaks at 368.6 and 374.6 eV were assigned to Ag(0) (Fig. 4(a)) (Xu et al.,
350 2011), and the splitting of the 3d doublet of Ag (6.0 eV) confirmed the presence of Ag(0)
351 (Chastain and King Jr, 1992; Xu et al., 2011).

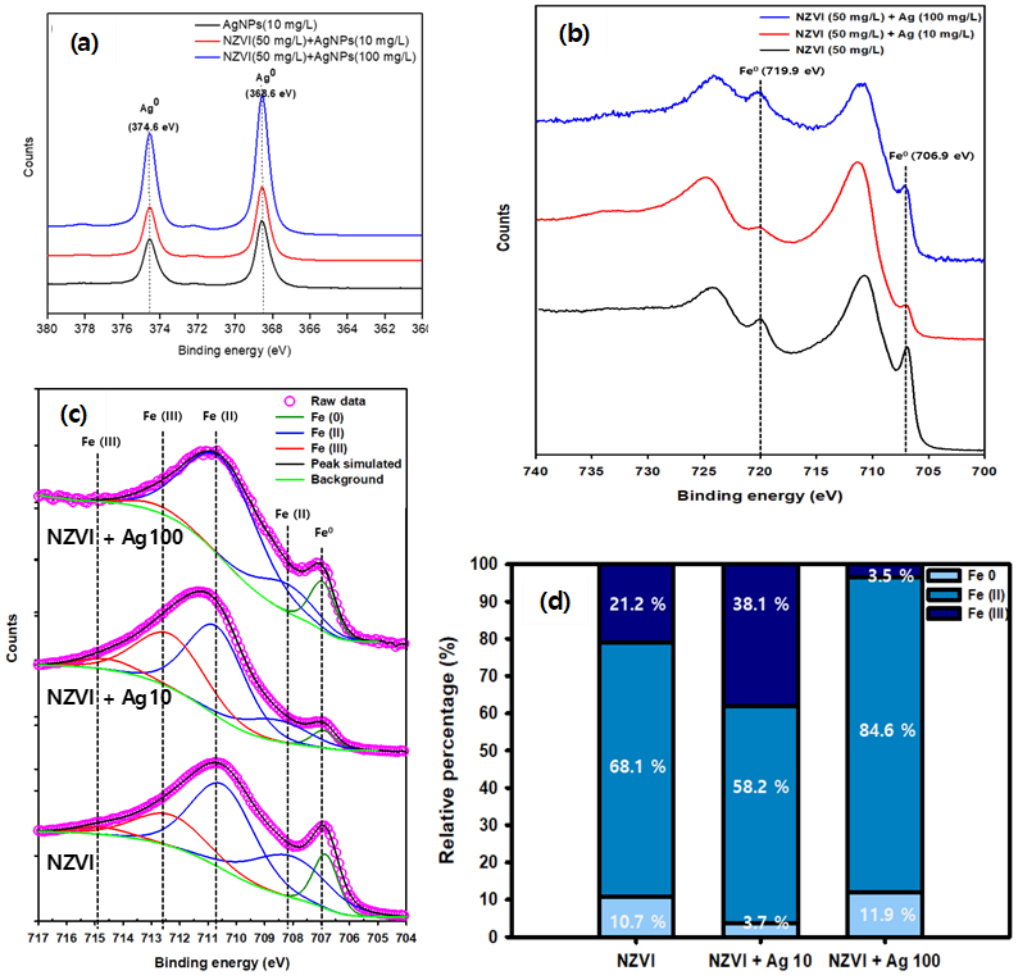

Figure 4. XPS spectra of (a) Ag(3d) in AgNP and NZVI-AgNP suspensions, (b) Fe(2p) in NZVI and NZVI-AgNP suspensions, (c) the corresponding deconvolution results of Fe($2p_{3/2}$) (705–717 eV), and (d) relative percentage of iron species.

In the pristine NZVI, two distinct peaks were observed at 719.9 and 706.9 eV, which corresponded to the Fe($2p_{1/2}$) and Fe($2p_{3/2}$) of Fe(0) (Luo et al., 2014), respectively (Fig. 4(b)). In the NZVI-AgNP suspension, Fe(0) peaks were enhanced, indicating the presence of more Fe(0) on the NZVI surface after AgNPs were introduced (Li et al., 2009). The XPS spectra of Fe(2p3/2) (Fig. 4(c)) showed five peaks at 706.9,

708.2–708.5, 710.3–710.7, 711.5–711.6, and 713.1–713.7 eV, which were assigned to the binding energies of Fe(0) (706.5–707.0 eV), Fe(II)–O (708.2–710.9 eV), and Fe(III)–O (711.0–714.0 eV). The proportion of Fe(0) (10.7%) and Fe(II) (68.1%) on the NZVI surfaces significantly decreased to 3.7% and 58.2% after adding 10 mg/L AgNPs, respectively (Fig. 4(d)). In contrast, their percentages dramatically increased to 11.9% and 84.6% in the sample of NZVI with 100 mg/L AgNPs. These results demonstrate that the presence of AgNPs decreased and increased the Fe(0) content on the NZVI surface, which are in agreement with the results of degradation kinetics in Fig. 2(b). This is also consistent with the TEM–EDS results (Fig. S8(c)), which showed a thinner oxide layer on the NZVI surface at a higher AgNP dose. Previous investigations have shown that the collision and friction between particles might occur in suspensions under stirring conditions (Xie and Luo, 2018). In addition, these particle-particle interactions become much stronger when both particle size and solid loading increased (Xie and Luo, 2018). In our systems, higher AgNP doses enabled homoaggregation and an increase in aggregate size (Fig. S11), likely inducing more collision between large-sized AgNP aggregates and NZVI. This phenomenon likely contributed to the peeling of the NZVI surface layer, which further resulted in the exposure of the NZVI inner core. These results suggest that a higher AgNP dose led to the partial removal of the iron oxide shell of NZVI through collisions between AgNP homoaggregates and NZVI. Self-assembled AgNPs with bigger sizes accelerated the peeling of the Fe oxide shell on the NZVI surface, thereby increasing the exposure of

383 inner Fe(0), and consequently, enhancing the *p*-NP removal. This also explains the
384 enhanced NZVI reactivity under an increasing dose of sand microparticles (Fig. S5).
385 As sand microparticles are inert and have a low surface area (0.06 m^2/g), the enhanced
386 NZVI reductive ability may be attributed to collision-driven processes in an aqueous
387 suspension.

388

389 *3.4. Effects of groundwater constituents on nanoparticles interaction and reactivity*

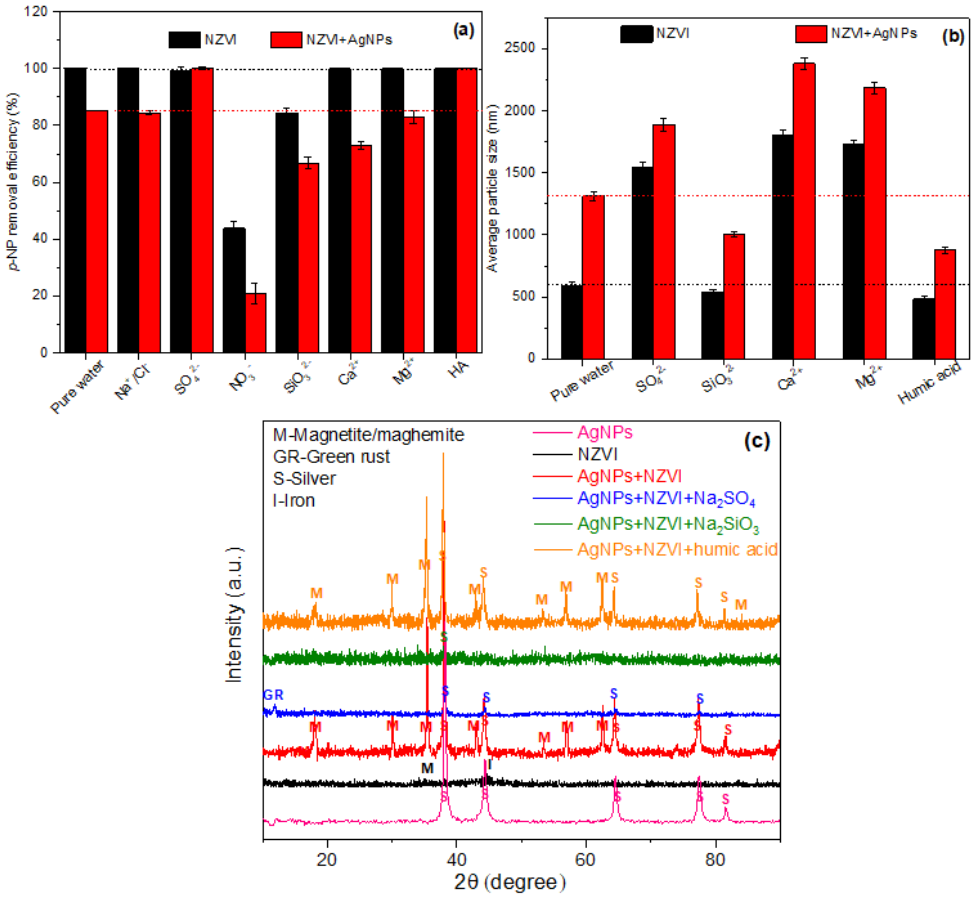

390

391 Figure 5. (a) Removal efficiencies of *p*-NP (2 h reaction) by NZVI and NZVI+AgNPs
392 in the presence of co-existing groundwater solutes; (b) Average particle size of NZVI

393 and AgNP–NZVI complexes in the presence of non-competing groundwater solutes; (c)
394 XRD pattern of the resulting products after the reaction of *p*-NP with non-competing
395 groundwater solutes. Experimental conditions: $[p\text{-NP}]_{initial}$ = 0.1 mM; [NZVI] = 50
396 mg/L; [AgNPs] = 10 mg/L; pH = 9.0±0.2; $[Na^+/Cl^-]$ = 5 mM; $[SO_4^{2-}]$ = 1 mM; $[NO_3^-]$
397 = 0.5 mM; $[SiO_3^{2-}]$ = 0.5 mM; $[Ca^{2+}]$ = 2 mM; $[Mg^{2+}]$ = 2 mM; and [HA] = 5 mg/L.
398
399 In the environment, the concentration of AgNPs is normally much lower than those
400 of NZVI used for remediation purposes (Su et al., 2013; McGillicuddy et al., 2018), the
401 inhibition effect of AgNPs to NZVI would be more significant in natural systems. To
402 evaluate the inhibition effects of AgNPs on the NZVI reactivity in conditions that
403 emulate natural systems, the *p*-NP reduction in NZVI (50 mg/L) and AgNP (10 mg/L)
404 suspensions was investigated in the presence of naturally occurring cations, anions, and
405 organic matter. Experiments were conducted with groundwater constituents and humic
406 acids (HAs) at levels similar to those encountered in real groundwater (Fig. 5(a))
407 (Edmunds and Shand, 2008). No impact of NaCl was observed. In the presence of most
408 groundwater solutes, NZVI exhibited good performance for *p*-NP removal, with 100%
409 removal over 2 h, except in the presence of NO_3^- (44%) and SiO_3^{2-} (84%). For NO_3^-,
410 the inhibitive result could be caused by a competitive reduction of NO_3^- by NZVI (Ryu
411 et al., 2011). Compared to NZVI-AgNPs in pure water (85%), the removal efficiency
412 of *p*-NP by the NZVI-AgNPs with NO_3^-, SiO_3^{2-}, Ca^{2+}, and Mg^{2+} decreased to 21%, 67%,
413 73%, and 83%, respectively. Furthermore, *p*-NP was completely removed over 2 h in

414 the presence of SO_4^{2-} and HA, which represents a better performance than that obtained
415 in pure water.

416 To further clarify the aggregation behavior of the particles, we measured the
417 average particle sizes of NZVI and AgNP–NZVI suspensions in the presence of SO_4^{2-},
418 SiO_3^{2-}, Ca^{2+}, Mg^{2+}, and HA (Fig. 5(b)). As expected, the particles sizes in the NZVI-
419 AgNP systems were higher than in systems without AgNPs, which was attributed to the
420 heteroaggregation between AgNPs and NZVI particles. Upon the introduction of Ca^{2+}
421 or Mg^{2+}, the particle size drastically increased from 593 nm to 1804 and 1727 nm in the
422 NZVI system, and from 1313 nm to 2382 and 2186 nm in the NZVI-AgNP system,
423 respectively. This was attributed to the particle surface charge screening (EDL
424 contraction) by Ca^{2+}/Mg^{2+} (Rogozhnikov, 2001). EDL contraction can decrease the
425 electrostatic or steric repulsive forces of the nanoparticles, thereby increasing
426 aggregation (Petosa et al., 2010) and further decreasing the NZVI reactivity (Ryu et al.,
427 2011). Moreover, Ca^{2+} and Mg^{2+} showed stronger inhibitive effects in NZVI-AgNPs
428 than in NZVI alone. In the presence of Ca^{2+} or Mg^{2+}, electrostatic repulsive forces
429 among particles (i.e., NZVI–NZVI, NZVI–AgNP, AgNP–AgNP) favored
430 homoaggregation and heteroaggregation, thus altering the NZVI reactivity.

431 In contrast, a decrease in the average particle size of NZVI (from 593 to 486 nm)
432 and NZVI-AgNPs (from 1313 to 877 nm) in the presence of HA was attributed to the
433 interactions of HA with the surfaces, which likely enhanced the electrostatic repulsion
434 decreased (Dong and Lo, 2013). This reduced particle aggregation, which enhanced the

435 removal of *p*-NP. The particle size decreased more for NZVI-AgNPs than for NZVI,
436 which suggests that less AgNPs were attached to NZVI surfaces, thereby providing a
437 lower inhibition effect of AgNPs in the presence of HA.

438 XRD analysis was also conducted to analyze the passivation byproducts of NZVI-
439 AgNPs after the reaction (Fig. 5(c)). The byproducts in the pure water system included
440 maghemite (γ-Fe_2O_3)/magnetite (Fe_3O_4) and silver (Ag(0)), which were attributed to
441 NZVI oxidation during the *p*-NP reduction (Xiong et al., 2018). Similarly, in the
442 presence of HA, maghemite/magnetite and silver (Ag(0)) phases were also detected
443 after *p*-NP removal. In contrast, green rust ($[Fe^{2+}_4Fe^{3+}_2(HO^-)_{12}]^{2+}\cdot[SO^{2-}_4\cdot 2H_2O]^{2-}$)
444 (Tahawy et al., 2021) and silver (Ag(0)) were detected in the presence of SO_4^{2-}.
445 Considering the relatively higher reactivity of green rust than that of magnetite
446 (Digiacomo et al., 2020; Usman et al., 2018), the enhanced *p*-NP removal in the NZVI-
447 AgNP-SO_4^{2-} system (Fig. 5(a)) was attributed to the generated green rust. For SiO_3^{2-}, a
448 weak peak of silver was identified as the final product, and there was no obvious Fe
449 phase detected in the XRD analysis. The absence of Fe phases might be attributed to
450 the amorphous coating of Si on the NZVI surface as previously reported, and the surface
451 coated Si would further reduce the amount of active surface sites available for
452 contaminants (Meng et al., 2002). Despite the lower particle size of NZVI-AgNP-SiO_3^{2-},
453 the reactivity of both NZVI and NZVI/AgNPs decreased drastically, which was
454 attributed to the strong binding of silicates to the NZVI surface.

455 **4. Conclusions**

Because of the increasing use of engineered nanoparticles (ENPs) in various industries and consumer items, ENPs are ubiquitously found in aquatic environments. However, little is known about the interactions among the co-existing ENPs in nature. This work showed for the first time how two typical engineered nanoparticles, nanoscale zero-valent iron (NZVI) and silver nanoparticles (AgNPs), interact and influence each other under environmentally-relevant conditions. First, we have investigated the potential interactions between AgNPs and NZVI particles using p-NP conversion into p-AP as a probe reaction. At a AgNP load of 10 mg/L, AgNPs covered the reactive NZVI surfaces, which decreased *p*-NP removal. Whereas at a AgNP load of 100 mg/L, the enhanced homoaggregation of AgNPs led to the exposure of the inner Fe(0) surface of NZVI because of particle collisions, which increased the *p*-NP removal. The same behavior was observed with nanosized TiO_2 particles and microsized quartz sand particles, thereby excluding the role of potential Ag^+ ions release, electron transfer process, and/or galvanic effect.

Second, the impact of groundwater constitutes has been evaluated, which showed contrasting effects depending on ion types and the binding affinities to Fe-oxides. These results revealed that not only AgNPs but also other nano/microsized particles (e.g. TiO_2 and quartz sand) may influence the NZVI reactivity, which will help to develop decision support and prediction tools for NZVI remediation technologies. Electron microscopic and X-ray spectroscopic investigations and DLVO calculations revealed that heteroaggregation of NZVI and AgNPs resulted in dramatic decrease of the NZVI

reactivity, while at higher AgNPs loading, collision between self-assembled aggregates of AgNPs and NZVI can improve the reductive ability of NZVI. These findings shed light on an overlooked aspect of interactions between co-existing nanoparticles, which could influence their fate and mobility in environmental settings. Owing to the increasing occurrence of NPs in aqueous environments, this work calls for more investigations of potential interactions between the co-occurring nanomaterials for accurate assessment of environmental associated risks.

Conflicts of interest

There are no conflicts to declare.

Acknowledgments

We would like to acknowledge the support from Korea Environment Industry & Technology Institute (KEITI) through "Subsurface Environmental Management (SEM) Project", funded by Korea Ministry of Environment (MOE) (2020002480006). We are also grateful for the assistance of Isabelle Soutrel (LC/UV) and Vincent Dorcet (THEMIS platform).

References

Abbas, Q., Yousaf, B., Amina, Ali, M.U., Munir, M.A.M., El-Naggar, A., Rinklebe, J., Naushad, M., 2020. Transformation pathways and fate of engineered nanoparticles (ENPs) in distinct interactive environmental compartments: A review. Environ. Int. 138, 105646.

Asghari, S., Johari, S.A., Ji, H.L., Yong, S.K., Yong, B.J., Choi, H.J., Min, C.M., Yu, I.J., 2012. Toxicity of various silver nanoparticles compared to silver ions in Daphnia magna. J. Nanobiotechnology 10(1), 1-11.

Auffan, M., Pedeutour, M., Rose, J., Masion, A., Ziarelli, F., Borschneck, D., Chaneac, C., Botta, C., Chaurand, P., Labille, J., Bottero, J.-Y., 2010. Structural Degradation at the Surface of a TiO2-Based Nanomaterial Used in Cosmetics. Environ. Sci. Technol. 44(7), 2689-2694.

Bae, S., Gim, S., Kim, H., Hanna, K., 2016. Effect of NaBH4 on properties of nanoscale zero-valent iron and its catalytic activity for reduction of p-nitrophenol. Appl. Catal., B 182, 541-549.

Bae, S., Hanna, K., 2015. Reactivity of nanoscale zero-valent iron in unbuffered systems: effect of pH and Fe (II) dissolution. Environ. Sci. Technol. 49(17), 10536-10543.

Bae, S., Lee, W., 2014. Influence of Riboflavin on Nanoscale Zero-Valent Iron Reactivity during the Degradation of Carbon Tetrachloride. Environ. Sci. Technol. 48(4), 2368-2376.

Brookins D.G. Eh- pH diagrams of geochemistry. Springer-Verlag, New York (1988).

Chastain, J., King Jr, R.C., 1992. Handbook of X-ray photoelectron spectroscopy. Perkin-Elmer Corporation 40, 221.

Danail, H., Ineke, M., 2009. Hazards and Risks of Engineered Nanoparticles for the Environment and Human Health. Sustainability 1(4), 1161-1161.

Deng, H., McShan, D., Zhang, Y., Sinha, S.S., Arslan, Z., Ray, P.C., Yu, H., 2016. Mechanistic study of the synergistic antibacterial activity of combined silver nanoparticles and common antibiotics. Environ. Sci. Technol. 50(16), 8840-8848.

Deng, J., Bae, S., Yoon, S., Pasturel, M., Marsac, R., Hanna, K., 2020. Adsorption capacity of the corrosion products of nanoscale zerovalent iron for emerging contaminants. Environ. Sci. Nano 7(12), 3773-3782.

Digiacomo, F., Tobler, D.J., Held, T., Neumann, T., 2020. Immobilization of Cr(VI) by sulphate green rust and sulphidized nanoscale zerovalent iron in sand media: batch and column studies. Geochem. Trans. 21(1), 8.

529 Dong, H., Lo, I.M.C., 2013. Influence of humic acid on the colloidal stability of surface-
530 modified nano zero-valent iron. Water Res. 47(1), 419-427.

531 Du, Y., Chen, H., Chen, R., Xu, N. 2004. Synthesis of p-aminophenol from p-
532 nitrophenol over nano-sized nickel catalysts. Appl. Catal. A-Gen 277(1), 259-264.

533 Echegoyen, Y., Nerín, C., 2013. Nanoparticle release from nano-silver antimicrobial
534 food containers. Food Chem. Toxicol. 62, 16-22.

535 Edmunds, W.M., Shand, P., 2008. Natural groundwater quality.

536 Hernández-Gordillo, A., Arroyo, M., Zanella, R., Rodríguez-González, V. 2014.
537 Photoconversion of 4-nitrophenol in the presence of hydrazine with AgNPs-TiO2
538 nanoparticles prepared by the sol–gel method. J. Hazard. Mater. 268, 84-91.

539 Joo, S.H., Feitz, A.J., Waite, T.D., 2004. Oxidative Degradation of the Carbothioate
540 Herbicide, Molinate, Using Nanoscale Zero-Valent Iron. Environ. Sci. Technol. 38(7),
541 2242-2247.0.799

542 Lai, B., Zhang, Y.-H., Li, R., Zhou, Y.-X., Wang, J., 2014. Influence of operating
543 temperature on the reduction of high concentration p-nitrophenol (PNP) by zero valent
544 iron (ZVI). Chem. Eng. J. 249, 143-152.

545 Li, S., Wang, W., Liang, F., Zhang, W.-x., 2017. Heavy metal removal using nanoscale
546 zero-valent iron (nZVI): Theory and application. J. Hazard. Mater. 322, 163-171.

547 Li, S., Yan, W., Zhang, W.-x., 2009. Solvent-free production of nanoscale zero-valent
548 iron (nZVI) with precision milling. Green Chem. 11(10), 1618-1626.

549 Lin, S., Cheng, Y., Liu, J., Wiesner, M.R., 2012. Polymeric Coatings on Silver
550 Nanoparticles Hinder Autoaggregation but Enhance Attachment to Uncoated Surfaces.
551 Langmuir 28(9), 4178-4186.

552 Liu, Y., Lowry, G.V., 2006. Effect of Particle Age (Fe0 Content) and Solution pH On
553 NZVI Reactivity: H2 Evolution and TCE Dechlorination. Environ. Sci. Technol.
554 40(19), 6085-6090.

555 Lorenz, C., Windler, L., von Goetz, N., Lehmann, R.P., Schuppler, M., Hungerbühler,
556 K., Heuberger, M., Nowack, B., 2012. Characterization of silver release from
557 commercially available functional (nano)textiles. Chemosphere 89(7), 817-824.

558 Luo, S., Lu, T., Peng, L., Shao, J., Zeng, Q., Gu, J.-D., 2014. Synthesis of nanoscale
559 zero-valent iron immobilized in alginate microcapsules for removal of Pb(ii) from
560 aqueous solution. J. Mater. Chem. A 2(37), 15463-15472.

561 Lützenkirchen, J., Preočanin, T. and Kallay, N. 2008. A macroscopic water structure
562 based model for describing charging phenomena at inert hydrophobic surfaces in
563 aqueous electrolyte solutions. Phys. Chem. Chem. Phys. 10(32), 4946-4955.

564 Mahdi, K.N.M., Peters, R.J.B., Klumpp, E., Bohme, S., Ploeg, M.v.d., Ritsema, C.,

565 Geissen, V., 2017. Silver nanoparticles in soil: Aqueous extraction combined with
566 single-particle ICP-MS for detection and characterization. Environ. Nanotechnol.
567 Monit. Manag. 7, 24-33.

568 McGillicuddy, E., Morrison, L., Cormican, M., Dockery, P., Morris, D., 2018. Activated
569 charcoal as a capture material for silver nanoparticles in environmental water samples.
570 Sci. Total Environ. 645, 356-362.

571 Meng, X., Korfiatis, G.P., Bang, S., Bang, K.W., 2002. Combined effects of anions on
572 arsenic removal by iron hydroxides. Toxicol. Lett. 133(1), 103-111.

573 Mueller, N.C., Braun, J., Bruns, J., Černík, M., Rissing, P., Nowack, R.B., 2012.
574 Application of nanoscale zero valent iron (NZVI) for groundwater remediation in
575 Europe. Environ. Sci. Pollut. Res. 19(2), 550-558.

576 Petosa, A.R., Jaisi, D.P., Quevedo, I.R., Elimelech, M., Tufenkji, N., 2010. Aggregation
577 and deposition of engineered nanomaterials in aquatic environments: role of
578 physicochemical interactions. Environ. Sci. Technol. 44(17), 6532-6549.

579 Phenrat, T., Thongboot, T., Lowry, G.V., 2016. Electromagnetic Induction of Zerovalent
580 Iron (ZVI) Powder and Nanoscale Zerovalent Iron (NZVI) Particles Enhances
581 Dechlorination of Trichloroethylene in Contaminated Groundwater and Soil: Proof of
582 Concept. Environ. Sci. Technol. 50(2), 872-880.

583 Poudel, M.B., Karki, H.P. and Kim, H.J. (2020) Silver nanoparticles decorated
584 molybdenum sulfide/tungstate oxide nanorods as high performance supercapacitor
585 electrode. Journal of Energy Storage 32, 101693.

586 Poudel, M.B. and Kim, H.J., 2022. Confinement of Zn-Mg-Al-layered double
587 hydroxide and α-Fe2O3 nanorods on hollow porous carbon nanofibers: A free-standing
588 electrode for solid-state symmetric supercapacitors. Chem. Eng. J. 429, 132345.

589 Poudel, M.B., Shin, M. and Joo Kim, H., 2022. Interface engineering of MIL-88 derived
590 MnFe-LDH and MnFe2O3 on three-dimensional carbon nanofibers for the efficient
591 adsorption of Cr(VI), Pb(II), and As(III) ions. Sep. Purif. Technol. 287, 120463.

592 Poudel, M.B., Shin, M. and Kim, H.J. (2021) Polyaniline-silver-manganese dioxide
593 nanorod ternary composite for asymmetric supercapacitor with remarkable
594 electrochemical performance. International Journal of Hydrogen Energy 46(1), 474-
595 485.

596 Rogozhnikov, N.A., 2001. Effect of Alkali Metal Cations on the EDL Structure at a
597 Gold Electrode in Alkali Solutions. Russ. J. Electrochem. 37(10), 1101-1107.

598 Ryu, A., Jeong, S.-W., Jang, A., Choi, H., 2011. Reduction of highly concentrated
599 nitrate using nanoscale zero-valent iron: Effects of aggregation and catalyst on
600 reactivity. Appl. Catal., B 105(1-2), 128-135.

601 Shen, W., Zhang, X., Huang, Q., Xu, Q., Song, W., 2014. Preparation of solid silver

602 nanoparticles for inkjet printed flexible electronics with high conductivity. Nanoscale
603 6(3), 1622-1628.

604 Sohn, K., Kang, S.W., Ahn, S., Woo, M., Yang, S.-K., 2006. Fe (0) nanoparticles for
605 nitrate reduction: stability, reactivity, and transformation. Environ. Sci. Technol. 40(17),
606 5514-5519.

607 Sridhar, R., Lakshminarayanan, R., Madhaiyan, K., Barathi, V.A., Lim, K.H.C.,
608 Ramakrishna, S., 2015. Electrosprayed nanoparticles and electrospun nanofibers based
609 on natural materials: applications in tissue regeneration, drug delivery and
610 pharmaceuticals. Chem. Soc. Rev. 44(3), 790-814.

611 Stefaniuk, M., Oleszczuk, P., Ok, Y.S., 2016. Review on nano zerovalent iron (nZVI):
612 From synthesis to environmental applications. Chem. Eng. J. 287, 618-632.

613 Su, C., Puls, R.W., Krug, T.A., Watling, M.T., O'Hara, S.K., Quinn, J.W., Ruiz, N.E.
614 2013. Travel distance and transformation of injected emulsified zerovalent iron
615 nanoparticles in the subsurface during two and half years. Water Research 47(12), 4095-
616 4106.

617 Syafiuddin, A., Salmiati, S., Hadibarata, T., Kueh, A.B.H., Salim, M.R., Zaini, M.A.A.,
618 2018. Silver Nanoparticles in the Water Environment in Malaysia: Inspection,
619 characterization, removal, modeling, and future perspective. Sci. Rep. 8(1), 1-15.

620 Tahawy, R., Doustkhah, E., Abdel-Aal, E.-S.A., Esmat, M., Farghaly, F.E., El-Hosainy,
621 H., Tsunoji, N., El-Hosiny, F.I., Yamauchi, Y., Assadi, M.H.N., Ide, Y., 2021.
622 Exceptionally stable green rust, a mixed-valent iron-layered double hydroxide, as an
623 efficient solar photocatalyst for H2 production from ammonia borane. Appl. Catal., B
624 286, 119854.

625 Tsarev, S., Collins, R.N., Ilton, E.S., Fahy, A., Waite, T.D., 2017. The short-term
626 reduction of uranium by nanoscale zero-valent iron (nZVI): role of oxide shell,
627 reduction mechanism and the formation of U(v)-carbonate phases. Environ. Sci. Nano
628 4(6), 1304-1313.

629 Usman, M., Byrne, J.M., Chaudhary, A., Orsetti, S., Hanna, K., Ruby, C., Kappler, A.,
630 Haderlein, S.B., 2018. Magnetite and Green Rust: Synthesis, Properties, and
631 Environmental Applications of Mixed-Valent Iron Minerals. Chem. Rev. 118(7), 3251-
632 3304.

633 Vilardi, G. 2019. Mathematical modelling of simultaneous nitrate and dissolved oxygen
634 reduction by Cu-nZVI using a bi-component shrinking core model. Powder Technol.
635 343, 613-618.

636 Vilardi, G., Parisi, M., Verdone, N. 2019. Simultaneous aggregation and oxidation of
637 nZVI in Rushton equipped agitated vessel: Experimental and modelling. Powder
638 Technol. 353, 238-246.

639 Vilardi, G. 2020. P-aminophenol catalysed production on supported nano-magnetite
640 particles in fixed-bed reactor: Kinetic modelling and scale-up. Chemosphere 250,
641 126237.

642 Wang, R., Dang, F., Liu, C., Wang, D.-j., Cui, P.-x., Yan, H.-j., Zhou, D.-m., 2019.
643 Heteroaggregation and dissolution of silver nanoparticles by iron oxide colloids under
644 environmentally relevant conditions.. Environ. Sci. Nano. 6(1), 195-206.

645 Wei, Y.-T., Wu, S.-C., Chou, C.-M., Che, C.-H., Tsai, S.-M., Lien, H.-L., 2010.
646 Influence of nanoscale zero-valent iron on geochemical properties of groundwater and
647 vinyl chloride degradation: A field case study. Water Res. 44(1), 131-140.

648 Xia, X., Ling, L., Zhang, W.-x., 2017. Genesis of pure Se(0) nano- and micro-structures
649 in wastewater with nanoscale zero-valent iron (nZVI). . Environ. Sci. Nano 4(1), 52-59.

650 Xie, L., Luo, Z.-H., 2018. Modeling and simulation of the influences of particle-particle
651 interactions on dense solid–liquid suspensions in stirred vessels. Chem. Eng. Sci. 176,
652 439-453.

653 Xiong, Z., Lai, B., Yang, P., 2018. Enhancing the efficiency of zero valent iron by
654 electrolysis: Performance and reaction mechanism. Chemosphere 194, 189-199.

655 Xu, F., Piett, C., Farkas, S., Qazzaz, M., Syed, N.I., 2013. Silver nanoparticles (AgNPs)
656 cause degeneration of cytoskeleton and disrupt synaptic machinery of cultured cortical
657 neurons. Mol. Brain 6(1), 29-29.

658 Xu, H., Shi, X., Ma, H., Lv, Y., Zhang, L., Mao, Z., 2011. The preparation and
659 antibacterial effects of dopa-cotton/AgNPs. Appl. Surf. Sci. 257(15), 6799-6803.

660 Yu, S.J., Yin, Y.G., Chao, J.B., Shen, M.H., Liu, J.F., 2014. Highly dynamic PVP-coated
661 silver nanoparticles in aquatic environments: chemical and morphology change induced
662 by oxidation of Ag(0) and reduction of Ag(+). Environ. Sci. Technol. 48(1), 403-411.

663 Zhu, X., Zhou, L., Li, Y., Han, B., Feng, Q., 2021. Rapid Degradation of Carbon
664 Tetrachloride by Microscale Ag/Fe Bimetallic Particles. Int. J. Env. Res. Public Health
665 18(4), 2124.

666 Zhuang, Y., Ahn, S., Seyfferth, A.L., Masue-Slowey, Y., Fendorf, S., Luthy, R.G., 2011.
667 Dehalogenation of polybrominated diphenyl ethers and polychlorinated biphenyl by
668 bimetallic, impregnated, and nanoscale zerovalent iron. Environ. Sci. Technol. 45(11),
669 4896-4903.

670